Bulk and monolayer thermoelectric and optical properties of anisotropic NbS$_2$Cl$_2$

Arul Raj Natarajan [a], Mayanak K. Gupta [b,c], Ranjan Mittal [b,c], V. Kanchana [a,*]

[a] *Department of Physics, Indian Institute of Technology Hyderabad, Kandi 502285, Sangareddy, Telangana, India*
[b] *Solid State Physics, Bhabha Atomic Research Centre Trombay, Mumbai, 400085, India*
[c] *Homi Bhabha National Institute, Anushaktinagar, Mumbai, 400094, India*

ARTICLE INFO

ABSTRACT

Recently, the chalcogenide-based materials are attracting the scientific community due to their promising thermoelectric properties. Monoclinic compounds of the chalcogenide class of materials are the least explored for thermoelectric and optoelectronic device applications. In our present study, we have taken NbS$_2$Cl$_2$ to analyse its electronic properties of bulk and monolayer to understand its electronic and thermal transport properties along with its optical properties, using the density functional theory framework. The investigated compound has direct bandgap values of 1.41 eV and 1.67 eV in its bulk and monolayer phases, respectively, making it a semiconductor. The lattice thermal conductivity(κ_l), being a crucial parameter for a thermoelectric material, is observed to be ultra-low along 'c' direction for the bulk (0.44 Wm/K) and the same along 'b' direction for monolayer (0.36 Wm/K). We also predict a great potential for nanostructuring with 72% reduction in the thermal conductivity for the crystal grain size of 10 nm. Further, carrier lifetimes for various concentrations and temperatures are estimated by incorporating different scattering mechanisms in the calculations, such as acoustic deformation scattering (ADP), ionized impurity scattering (IMP) and polar optical scattering (POP). Based on thermoelectric performance, we predict n-type doping would be more favourable. At 700 K, n-type bulk has a maximum thermoelectric performance (ZT) of 0.4, higher than the well-known monoclinic GaTe (0.24) TE material. In addition, the calculated absorption coefficient reveals the optical anisotropy. The predicted absorption coefficients for bulk and monolayer in the visible range are 7.5×10^5/cm and 3×10^5/cm, respectively. The current work highlights its extremely low thermal conductivity and significant absorption coefficients, which could lead to future applications in thermoelectric and optical devices.

1. Introduction

Growing population and industrialization demands enormous energy production. But, as fossil fuels are depleting rapidly, search for alternative sources that do not pollute the environment is inevitable [1]. Thermoelectric and solar cells are both environmental friendly and alternative energy sources to fossil fuels [2,3]. The efficiency of thermoelectric materials as determined by an dimensionless quantity, figure of merit is,

$$ZT = \frac{S^2\sigma}{(k_l + k_e)}T \tag{1}$$

where 'S' is Seebeck coefficient or thermopower, 'σ' is electrical conductivity, 'T' is temperature and 'k_l' and 'k_e' are the lattice and electronic contribution to the thermal conductivity respectively [4]. A good thermoelectric material should have a high Seebeck coefficient, low heat conductivity, and high electrical conductivity. The power factor($S^2\sigma$)

is crucial in assessing how efficient a material is. Due to the conflicting needs of material characteristics for enhancing S and σ simultaneously, increasing the power factor is incredibly challenging. Similarly, κ_e and σ are related through Wiedemann–Franz law [5]. As a result, the electronic thermoelectric coefficients S, κ_e and σ are all independent on each other. Therefore, tuning one without impacting the others is extremely challenging [6]. However, κ_l is independent of electronic TE coefficients, we can improve the figure of merit ZT by lowering it [7]. Because of their various application, materials with anisotropic thermoelectric characteristics have attracted much interest [8–11]. It might be possible to achieve a high thermopower and low thermal conductivity using layered materials [7,9,10,12]. Large phonon anharmonicity occurs at the interface between consecutive layers, resulting in increased phonon scattering and decreased lattice heat conductivity between layers which enhances the figure of merit ZT [8].

Nanostructuring is an excellent and widely used method for improving thermoelectric characteristics because it increases phonon scattering while lowering heat conductivity [13–15]. Generally, the chalcogen-based materials are promising thermoelectric materials [16–18]. According to the literature, Bi_2Te_3 is well-known TE material with high ZT [19–21]. However, because Te is expensive, toxic, and a scarce material, its usage in large-scale applications is not affordable. As a result, one of the ongoing primary objectives in TE research is to produce Te-free alternative materials. Furthermore, due to their low symmetry, monoclinic layered structures exhibit a highly anisotropic behaviour and have been reported to have excellent thermoelectric efficiency (ZT). For example, recently, Ga_2O_3[22,23], ZrS_3[9], GaTe and $LiZnS_3$[24] are reported as promising TE materials.

Multiple applications with a single source are gaining popularity these days, and also it motivates the experimentalists [25–28]. Some materials, such as PbTe [29,30], Ga_2O_3[22,23,31], InP_3[32] etc., have remarkable combined thermoelectric and optical properties, as reported in recent literature.

The optical characteristics of a material with a semiconducting nature and a direct bandgap are excellent. The absorption coefficient of a material, in particular, provides information on the material's optimal solar energy conversion efficiency, which is vital for the material's practical application in a solar cell [33].

Only a few studies have compared the TE and optical properties of bulk and monolayer materials [34]. The work is divided into three sections: Section 2 presents the computational details and Section 3 includes the results and discussions. The work is concluded in Section 4.

2. Computational details

The Vienna Ab-initio Simulation Package (VASP) tool is used to compute the structural relaxation, self-consistency, transport, and optical properties [35–38]. The exchange–correlation effects are solved by the Generalized Gradient Approximation(GGA) with Perdew–Burke–Ernzerhof(PBE) functionals [39]. We used the 600 eV energy cut-off for convergence and to avoid pulley stress. The tolerance values for energy and force convergence in structural optimization are 10^{-6} eV and 0.01 eV/Å, respectively. The monoclinic structures are relaxed using a Monkhorst–Pack grid with $11 \times 6 \times 11$ kpoints for bulk and $11 \times 6 \times 1$ for monolayer [40]. A vacuum spacing of 20 Å thickness is used for monolayer NbS_2Cl_2 along the 'c' direction. The phonopy code and the VASP-implemented Density Functional Perturbation Theory (DFPT) were used to calculate phonon dispersion [41]. The finite displacement method is employed to calculate the lattice thermal conductivity using phono3py package [42].

In general, the Boltzmann transport theory is used in transportation studies with the constant relaxation time approximation (CSTA), which does not consider various scattering mechanisms independently. Different scattering mechanisms, such as ADP, IMP, and POP, have recently been implemented in the AMSET code [43], which is used to calculate the absolute values of thermoelectric coefficients through Boltzmann transport equation. The net relaxation rates are added by Mattheissen's rule,

$$\frac{1}{\tau_e} = \frac{1}{\tau^{ADP}} + \frac{1}{\tau^{IMP}} + \frac{1}{\tau^{POP}} \tag{2}$$

The scattering rates are calculated using Fermi's golden rule as

$$\tau_{n\mathbf{k} \to m\mathbf{k+q}}^{-1} = \frac{2\pi}{h} \left| g_{nm} \right|^2 \delta(\epsilon_{n\mathbf{k}} - \epsilon_{m\mathbf{k+q}}) \tag{3}$$

where $n\mathbf{k}$ is a initial wavevector and $m\mathbf{k+q}$ final wavevector after scattering. ϵ and g are the carrier energy and coupling matrix element, respectively. δ is Dirac delta function which ensures energy is conserved during scattering process. Coupling matrix elements represents strength of electron–phonon interactions due to various mechanisms such as ADP, IMP and POP. These matrix elements are calculated as,

$$g_{nm}^{ADP}(k, q) = \left[\frac{K_B T \alpha_v^2}{B_0} \right]^{1/2} < \psi_{mk+q} | \psi_{nk} > \tag{4}$$

Table 1
Experimental and optimized lattice parameters of NbS_2Cl_2.

Lattice parameters	Expt	LDA	GGA	DFT-D2	DFT-D3
a (Å)	6.26	6.09	6.35	6.29	6.27
b (Å)	11.09	10.98	11.17	11.15	11.13
c (Å)	6.69	6.41	7.38	6.78	6.70
V (Å³)	434.08	404.83	495.44	444.48	437.02

Table 2
Experimental [44] and calculated bond length difference between different atoms in NbS_2Cl_2.

	Nb-Nb	S-S	Nb-2S(1)	Nb-2S(2)	Nb-2Cl(1)	Nb-2Cl(2)
Expt(Å)	2.87	1.99	2.48	2.48	2.59	2.61
Calc(Å)	2.88	2.01	2.49	2.48	2.57	2.60

$$g_{nm}^{IMP}(k, q) = \left[\frac{n_{ii} Z^2 e^2}{\epsilon_0} \right]^{1/2} \frac{< \psi_{mk+q} | \psi_{nk} >}{|q|^2 + \beta^2} \tag{5}$$

$$g_{nm}^{POP}(k, q) = \left[\frac{\hbar \omega_{po}}{2} \left(\frac{1}{\epsilon_\infty} - \frac{1}{\epsilon_0} \right) \right]^{1/2} \frac{< \psi_{mk+q} | \psi_{nk} >}{|q|} \tag{6}$$

Here, the dielectric constants ϵ, phonon frequency ω, bulk modulus B_0, deformation potential α, were all calculated from First-principle methods.

3. Results and discussion

3.1. Structural and electronic properties

The bulk and monolayer(ML) structures are depicted in Fig. 1. NbS_2Cl_2 crystallizes in a monoclinic structure, and the space group is C2/m having a D_{2h} symmetry [44]. Bulk NbS_2Cl_2 crystallizes in a layered structure with weak van der Waal's interaction among the layers. Nb atoms appear in pairs in the NbS_2Cl_2 monolayer, and each Nb–Nb pair is coupled to four S atoms to form a cage-shaped Nb_2S_4 unit. The octahedral Nb_2S_4 fragments are linked by bridging halogen atoms into layers.

We relax the crystal structure using LDA and GGA exchange–correlation functionals. We discovered a significant difference between the theoretical and experimental volumes which are given in Table 1. So, we applied van der Waal's effect and found that the values estimated using Grimme's zero damping DFT-D3 approach is in good agreement with the experimental lattice parameters. The interlayer distance between two layers is 3.51 Å, similar to that of state-of-art thermoelectric materials SnS_2(3.6 Å) and $SnSe_2$(3.58 Å) [45]. The estimated bonding distances are also consistent with the experimental results which are given in Table 2.

The electronic bandstructure characteristics of bulk and ML NbS_2Cl_2 are calculated by PBE functional, which are depicted in Fig. 2(a) and Fig. 2(b). Based on the calculated electronic bandstructure, we observe a band gap of 1.41 eV for bulk and 1.67 eV for monolayer. The increment in bandgap value of monolayer is due to quantum confinement effect, a well known consequence of dimensional reduction. The high symmetry points 'M' and 'Y' with direct bandgap are where the valence band maximum (VBM) and conduction band minimum (CBM) for bulk and monolayer, respectively, are positioned. Figs. 2(c) and 2(d) depict the total and partial density of states for bulk and monolayer, respectively. We can see that the Nb-d state contributes more to the valence band than the S-p and Cl-p states. In the conduction band near the Fermi level, S-p contributes more than Nb-d and Cl-p. Flat bands in the VBM and dispersive bands in the CBM disclose the possibility of potential TE materials, that will be analysed in the coming section.
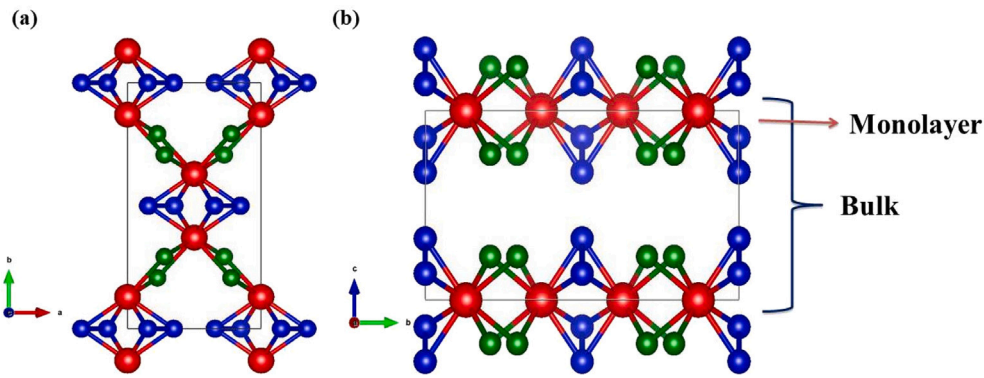
Fig. 1. The fully relaxed geometry of NbS_2Cl_2 structure: (a) side and (b) top views. The atoms of Nb, S and Cl are depicted as red, blue and green, respectively. (For interpretation of the references to colour in this figure legend, the reader is referred to the web version of this article.)
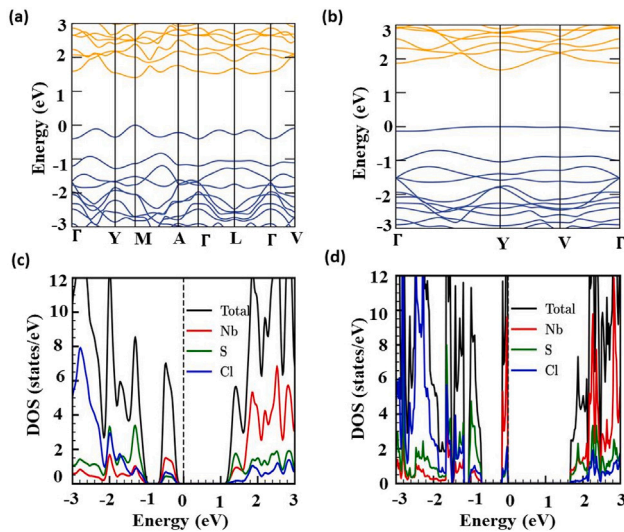

Fig. 2. The calculated electronic bandstructure and density of states for the bulk (a, c) and monolayer (b, d) NbS_2Cl_2.
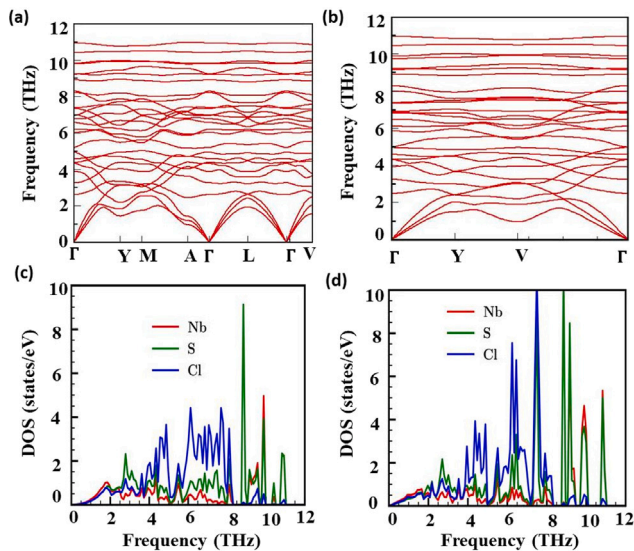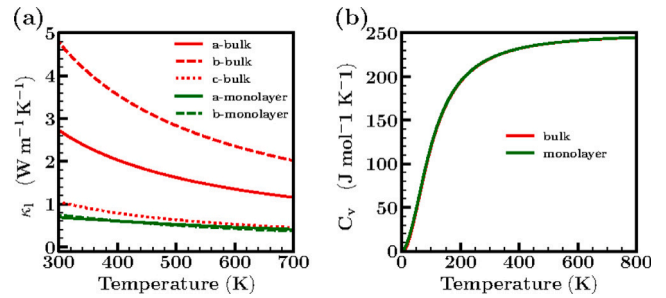

Fig. 4. The calculated lattice thermal conductivity (a) and specific heat capacity (b) for NbS_2Cl_2.
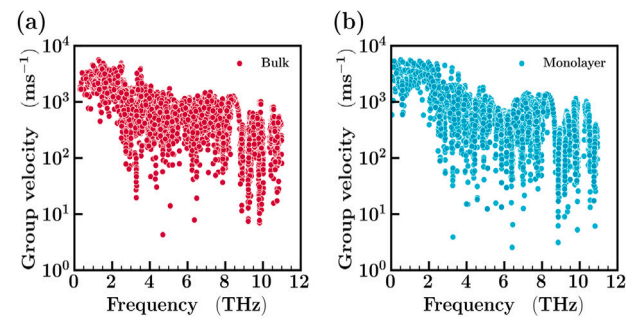

Fig. 5. The calculated phonon group velocity for bulk (a) and monolayer (b) of NbS_2Cl_2.

Fig. 3. The calculated phonon dispersion and phonon density of states for the bulk (a, c) and monolayer (b, d) NbS_2Cl_2.

3.2. Phonon and thermal transport properties

The estimated phonon bandstructure and phonon density of states of bulk and monolayer NbS_2Cl_2 are shown in Fig. 3. The investigated compound's dynamical stability is confirmed by the lack of imaginary modes in bulk and monolayer. In the phonon band spectrum, monolayer has a more flat band nature than bulk, indicating that monolayer's lattice thermal conductivity might be low. Because the atomic sizes are so similar, practically all of the atoms' contributions to the phonon density of states are the same. Fig. 4(a) shows the calculated κ_l of NbS_2Cl_2 bulk and monolayer. The κ_l for NbS_2Cl_2 bulk are 1.56, 2.01, and 0.45 W/mK in the 'a', 'b' and 'c' directions, respectively. However, the κ_l for monolayer NbS_2Cl_2 are only 0.40 and 0.36 W/mK in the 'a' and 'b' directions, respectively, at 700 K. The calculated κ_l values of both bulk and monolayer for different directions are given in Table 3. Because of its layered nature, bulk lattice κ_l is lower in out-of-plane than the in-plane directions. The calculated lattice thermal conductivity plot reveals a large anisotropy in bulk. For example, the κ_l of the 'b'
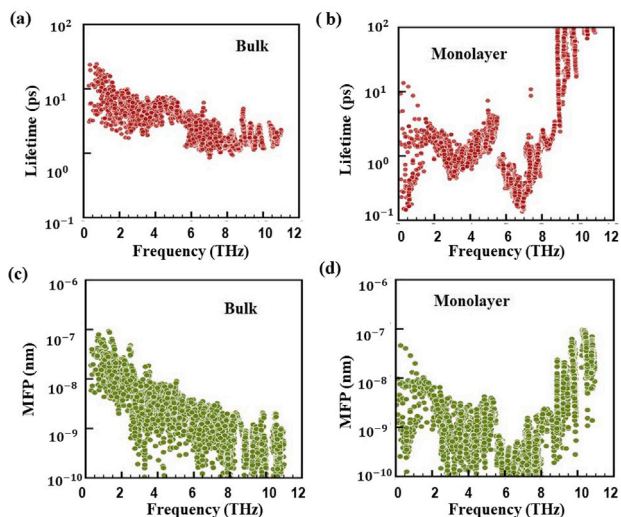
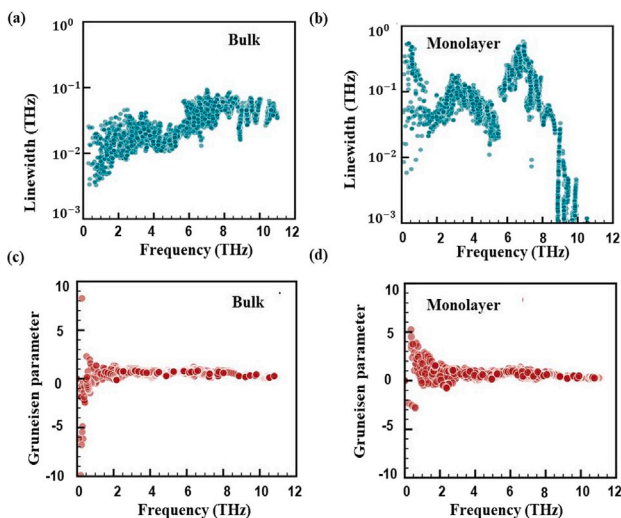**Fig. 6.** The calculated phonon lifetime (a, b) and mean-free path (c, d) of NbS_2Cl_2.

Fig. 7. The calculated linewidth (a, b) and Grüneisen parameter (c, d) of NbS_2Cl_2.

Table 3
The calculated lattice thermal conductivity (κ_l (in units $Wm^{-1}K^{-1}$)) of NbS_2Cl_2.

	Bulk			Monolayer	
	a	b	c	a	b
300 K	2.72	4.78	1.05	0.69	0.74
500 K	1.62	2.83	0.63	0.52	0.5
700 K	1.56	2.01	0.45	0.4	0.36

direction is 5 times higher than that of the 'c' direction. Similarly, the κ_l along the 'a' direction is 3.5 times higher than the 'c' direction in bulk at 700 K. In order to explain the observed behaviour of lower κ_l as well as the reduction of κ_l from bulk to monolayer, we looked into the various phonon properties of individual modes pertaining to lattice heat conductivity.

The lattice thermal conductivity is explained by the kinetic theory of phonon gas,

$$\kappa_l = \frac{1}{3} C_v v_g^2 \tau \tag{7}$$

Where C_v, V_g and τ are the specific heat capacity, average group velocity and average relaxation time of phonons, respectively. The estimated heat capacities of bulk and monolayer are shown in Fig. 4(b).
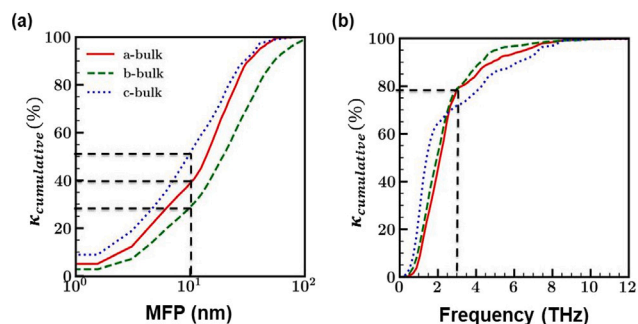

Fig. 8. The calculated cumulative lattice thermal conductivity versus (a) MFP and (b) frequency for bulk structure of NbS_2Cl_2.

We observe that there is no significant difference between their specific heat capacities. Likewise, the phonon group velocities of individual modes versus frequency is shown in Fig. 5. As we can observe for both bulk and monolayer, the group velocity values of a majority of the phonon modes are concentrated between $10^2 - 10^4$ m/s range and we have not noticed any significant differences in their group velocities also. Therefore, the observed large difference in κ_l between the bulk and monolayer should be less influenced by their corresponding heat capacities as well as group velocities. We have also calculated lifetimes(τ) of phonon modes for bulk and monolayer NbS_2Cl_2 which are shown in Fig. 6(a) and Fig. 6(b). While most of the bulk phonons modes' lifetimes are above 1 ps, the same for monolayers' modes are less than 1 ps at low frequency range. Therefore we can deduce that the significant difference in observed κ_l between the bulk and monolayer is due to their corresponding phonon lifetimes. Similar behaviour has been seen in the mean free path, as depicted in Fig. 6(c) and Fig. 6(d). The mean free path of phonon modes, being defined as $\Lambda = v_g \tau$, are much less for monolayer than bulk especially for acoustic and low frequency optical modes. These observations suggest that the monolayer has higher phonon scattering and thereby larger anharmonicity than the bulk, which could be the reason behind low lattice thermal conductivity of monolayer. We have also plotted the linewidth(Γ) of phonon modes from the relationship $\tau = 1/2\Gamma$, in Fig. 7(a) and Fig. 7(b) to understand the origin of such low lifetimes. The linewidths provide information regarding phonon modes' anharmonicity [46]. The monolayer's linewidth has more modes than the bulk, which considerably reduces the monolayer's phonon lifetime. Therefore, in order to analyse the difference in anharmonicity, we have plotted the Grüneisen parameters which can be used to analyse a crystal' anharmonic interactions in a quantitative way, as shown in Fig. 7(c) and Fig. 7(d). The large Grüneisen parameters, which are found mostly in the low-frequency range, are critical for heat transport due to phonons [47]. As we can see from the plots, the monolayer has a stronger Grüneisen parameter than bulk, indicating that monolayer has a higher anharmonicity than bulk.

For a practical material, the size dependence of thermal conductivity is a critical concern. Fig. 8(a) depicts the cumulative effect of bulk κ_l versus MFP for 300 K. The increment of cumulative κ_l along the 'b' direction when the MFP increases is significantly lower than along the 'a' and 'c' directions. Moreover, by reducing the grain size of the material to 10 nm, we can decrease the κ_l along the 'a', 'b' and 'c' direction by 60%, 50% and 72%, respectively. Therefore, nanostructuring is a viable method for lowering lattice thermal conductivity and hence an efficient way to improve the ZT for our studied compound. Fig. 8(b) depicts the cumulative κ_l versus phonon frequency at 300 K. We can see that modes below 3 THz contribute 80% in cumulative κ_l, indicating that the majority of heat transfer in NbS_2Cl_2 occurs in the acoustic and low-frequency optical modes.
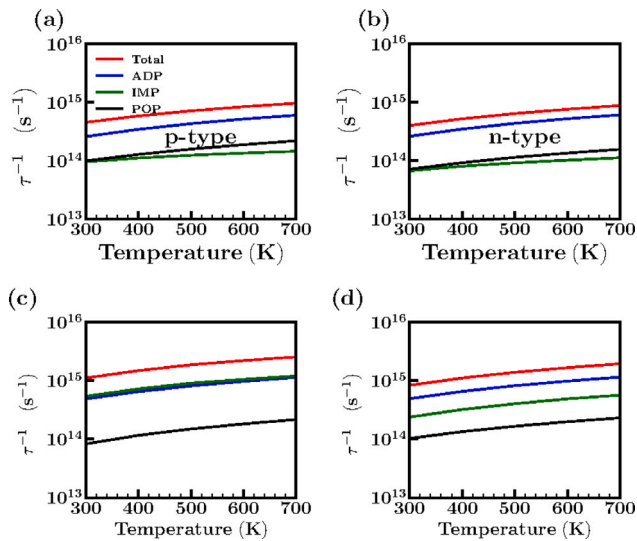
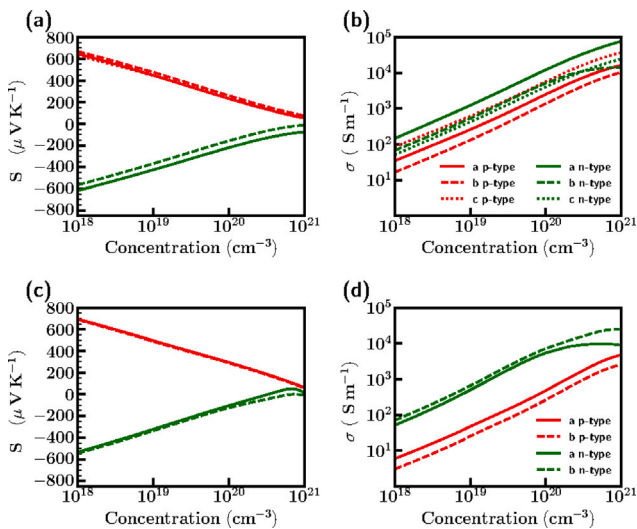**Fig. 9.** The Scattering rates as a function of temperature bulk (a, b) and monolayer (c, d) of NbS$_2$Cl$_2$.

Fig. 10. The calculated Seebeck coefficient for bulk (a, b) and monolayer (c, d) of NbS$_2$Cl$_2$.

3.3. Electronic transport properties and figure of merit

The computed electronic thermoelectric characteristics for bulk and monolayer NbS$_2$Cl$_2$ are discussed in this section. We calculated the different scattering rates, such as ADP, IMP and POP, for investigated compounds at a concentration of around 10^{19} cm^{-3}, shown in Fig. 9. We could not see any variation in IMP scattering with temperature as it purely depend upon the doping concentration. ADP and POP both dominate in low and high-temperature regime, respectively but in our case, ADP is contributing to a larger extent to total scattering effects throughout the temperature range. This might be due to the centrosymmetric symmetry of NbS$_2$Cl$_2$, which is minimizing the role of POP even at high temperature [43]. Both bulk and monolayer scattering rates are dominated by p-type. The monolayer's total scattering rates are higher than the bulk. We have tabulated the material parameters needed for the AMSET calculations in Table 4.

The estimated seebeck coefficient(S) and electrical conductivity(σ) of bulk and monolayer at 300 K are shown in Fig. 10. It is crucial to analyse the transport properties along all three crystal directions, since
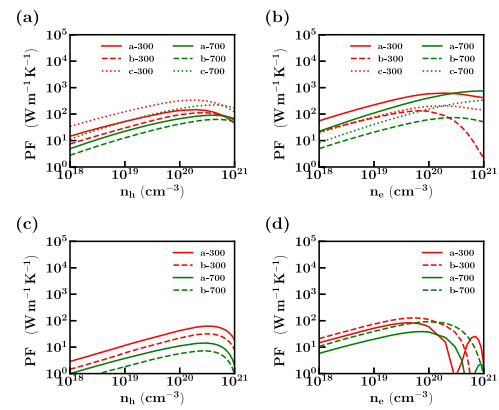

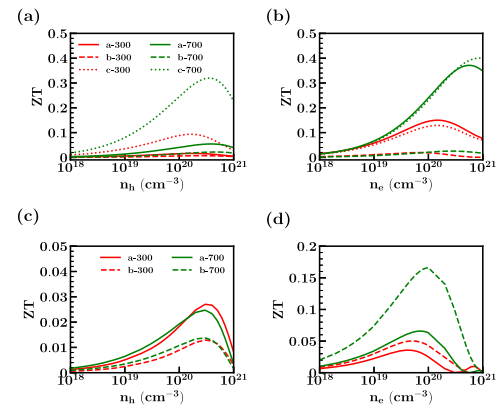**Fig. 11.** The calculated power factor for bulk (a, b) and monolayer (c, d) of NbS$_2$Cl$_2$.

Fig. 12. The calculated figure of merit (ZT) for bulk (a, b) and monolayer (c, d) of NbS$_2$Cl$_2$.

our compound is monoclinic. The high S is observed in 'b' direction for p-type and low for n-type in the same direction. The seebeck coefficient of both bulk and monolayers are not varying much. The maximum S is observed around $500 \mu V/K$ in optimum doping concentration range 10^{19} cm^{-3} at 300 K in p-type monolayer. In general, the thermopower is favourable for hole doping compared to electron doping. The electrical conductivity of electron concentration is higher than hole concentration in both bulk and monolayer. For example, the σ_e of bulk is 12.41×10^2 S/m in 'a' direction and 6.17×10^2 S/m in the 'c' direction for hole concentration and electron concentration, respectively.

The power factor(PF) of both bulk and ML is depicted in Fig. 11. The PF of electrons are higher than holes which is reflecting from the electrical conductivity. The bulk PF is higher than monolayer, for instance, the maximum PF is observed along 'a' direction is 223 W/mk in n-type bulk. The thermoelectric performance ZT is shown in Fig. 12. The ZT of bulk is higher than the monolayer. In particular, the ZT of n-type is higher than p-type for both bulk and monolayer. The maximum ZT observed in bulk is 0.32 for p-type and 0.4 for n-type along 'c' direction at 700 K. For ZT of the monolayer is found to be 0.024 for p-type along 'a' direction and 0.17 for n-type along 'b' direction at 700 K.

3.4. Optical properties

To explore the optoelectronic device applications, we have calculated optical properties of studied compounds. For the energy range of 0–10 eV, the optical characteristics of the examined compound are evaluated. The complex dielectric function is

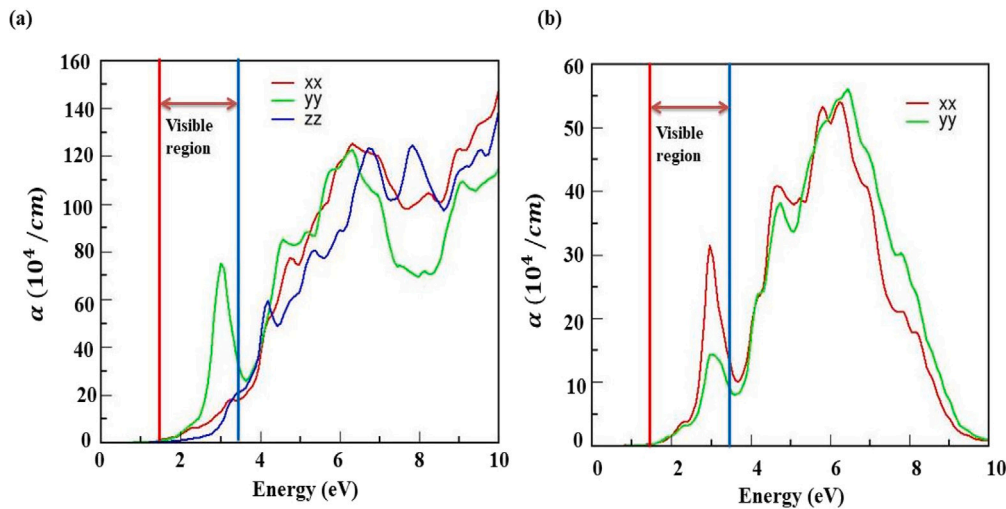$$\epsilon(\omega) = \epsilon_1(\omega) + i\epsilon_2(\omega) \tag{8}$$

(a)

(b)

Fig. 13. The calculated optical absorption coefficient bulk (a) and monolayer (b) of NbS_2Cl_2.

Table 4

Materials parameters used to compute scatterings rates of NbS_2Cl_2. $\epsilon_{s,ij}$ and $\epsilon_{\infty,ij}$ are the static and high-frequency dielectric constants in ϵ_0. ω_{po} is the effective polar phonon frequency given in THz.

	$\epsilon_{s,11}$	$\epsilon_{s,22}$	$\epsilon_{s,33}$	$\epsilon_{\infty,11}$	$\epsilon_{\infty,22}$	$\epsilon_{\infty,33}$	ω_{po}
Bulk	7.82	7.49	4.36	5.66	6.27	4.16	7.40
Monolayer	2.68	2.56	–	2.32	2.40	–	7.30

where ϵ_1 is the real part and ϵ_2 is the imaginary part of the dielectric function [48].

When it comes to optoelectronic applications, the material's optical absorption is crucial. The equation used to calculate the optical absorption coefficient(α) from,

$$\alpha(\omega) = \sqrt{2}\frac{\omega}{c}\left[\sqrt{\epsilon_1^2(\omega) + \epsilon_2^2(\omega)} - \epsilon_1(\omega)\right]^{1/2} \tag{9}$$

The calculated optical absorption coefficient for bulk and monolayer of NbS_2Cl_2 is shown in Fig. 13. The sharp peak absorption coefficient in the visible region is noticed in 7.5×10^5/cm along y-direction and 3×10^5/cm along x-direction for bulk and monolayer at 3 eV, respectively. It is obvious that the absorption coefficients for materials are high ($\approx 10^5$) which can be used in optical devices [49]. The electronic transition of Nb-d states in the VBM to S-p and Cl-p states in the CBM produced the peak. The observed absorption coefficient indicates that the studied compound is viable for photovoltaic applications.

4. Conclusion

We have performed a detailed investigation of electron and phonon thermoelectric characteristics and optical characteristics for both bulk and monolayer. The experimentalist would be drawn towards the low κ_l that results from dimensional reduction since it can be further decreased by nanostructuring. The Grüneisen parameter explains the phonon's anharmonicity. We have calculated efficient electronic transport using different scattering potentials such as ADP, IMP and POP. The figure of merit ZT is 0.4 in n-type material, and we can further improve by electron doping in bulk. The first peak in the optical absorption coefficient is noticed in the visible region. The directional dependent promising TE and optical characteristics of bulk and monolayer NbS_2Cl_2 are suitable for future thermoelectric and optical device applications.

CRediT authorship contribution statement

Arul Raj Natarajan: Formal analysis, Writing – original draft. **Mayanak K. Gupta:** Writing – review & editing. **Ranjan Mittal:** Formal analysis, Writing – review & editing. **V. Kanchana:** Conceptualization, Formal analysis, Writing – review & editing, supervision.

Declaration of competing interest

The authors declare that they have no known competing financial interests or personal relationships that could have appeared to influence the work reported in this paper.

Data availability

Data will be made available on request.

Acknowledgements

References

[1] A.F. Ioffe, in: A. Gelbtuch, H.J. Goldsmid (Eds.), Semiconductor Thermoelements and Thermoelectric Cooling, Infosearch, London, 1957.
[2] C. Wood, Materials for thermoelectric energy conversion, Rep. Progr. Phys. 51 (1988) 459.
[3] J.H. Yang, T. Caillat, Thermoelectric materials for space and automotive power generation, MRS. Bull. 31 (2006) 224.
[4] G.J. Snyder, E.S. Toberer, Complex thermoelectric materials, Nature Mater. 7 (2008) 101–105.
[5] A.J. Minnich, M.S. Dresselhaus, Z.F. Ren, Bulk nanostructured thermoelectric materials: current research and future prospects, G. Chen, Energy Environ. Sci. 2 (2009) 466–479.
[6] J.Y. Yang, W. Zhang, M. Hu, Decoupling thermal and electrical transport in α-MgAgSb with synergic pressure and doping strategy, J. Appl. Phys. 125 (2019) 205105.
[7] L.D. Hicks, M.S. Dresselhaus, Thermoelectric figure of merit of a one-dimensional conductor, Phys. Rev. B 47 (1993) 631–634.
[8] N. Wang, M. Li, H. Xiao, X. Zu L. Qiao, Layered LaCuOSe: A Promising anisotropic thermoelectric material, Phys. Rev. A 92 (2020) 024038.
[9] C. Wang, C. Zheng G. Gao, Bulk and Monolayer ZrS_3 as Promising anisotropic thermoelectric materials: A comparative study, J. Phys. Chem. C 124 (2020) 6536–6543.
[10] F.Q. Wang, F. Guo, Q. Wang, Y. Kawazoe, P. Jena, Exceptional thermoelectric properties of layered $GeAs_2$, J. Chem. Mater. 29 (2019) 9300–9307.

[11] X. Li, B. Xu, G. Yu, L. Xue, L. Yi, Anisotropic optical and thermoelectric properties of In_4Se_3 and In_4Te_3, J. Appl. Phys. 113 (2013) 203502.

[12] R. Guo, X. Wang, Y. Kuang, B. Huang, First-principles study of anisotropic thermoelectric transport properties of IV-VI semiconductor compounds SnSe and SnS, Phys. Rev. B 92 (2015) 115202.

[13] J. Mao, Z. Liu, Z. Ren, Size effect in thermoelectric materials, npj Quantum Mater. 1 (2016) 16028.

[14] L. Yang, Z.G. Chen, G. Han, M. Hong, Y. Zou, J. Zou, High-performance thermo-electric Cu_2Se nanoplates through nanostructure engineering, Nano Energy 16 (2015) 367–374.

[15] J. Zhang, D. Wu, D. He, D. Feng, M. Yin, X. Qin, J. He, Extraordinary thermo-electric performance realized in n-type PbTe through multiphase nanostructure engineering, Adv. Mater. 29 (2017) 1703148.

[16] J.R. Sootsman, D.Y. Chung, M.G. Kanatzidis, New and old concepts in thermoelectric materials, Angew. Chem. Int. Edn 48 (2009) 8616–8639.

[17] T.R. Wei, Y. Qin, T. Deng, Q. Song, B. Jiang, R. Liu, P. Qiu, X. Shi, L. Chen, Copper chalcogenide thermoelectric materials, Sci. China Mater. 62 (2019) 8–24.

[18] S. Roychowdhury, M. Samanta, S. Perumal, K. Biswas, Germanium Chalco-genide thermoelectrics: Electronic structure modulation and low lattice thermal conductivity, Chem. Mater. 30 (2018) 5799–5813.

[19] R. Venkatasubramanian, E. Siivola, T. Colpitts, B. O'Quinn, Thin-film thermo-electric devices with high room-temperature figures of merit, Nature 413 (2001) 597.

[20] T.M. Tritt, Holey and unholey semiconductors, Science 283 (1999) 804–805.

[21] B. Poudel, Q. Hao, Y. Ma, Y. Lan, A. Minnich, B. Yu, X. Yan, D. Wang, A. Muto, D. Vashaee, X. Chen, J. Liu, M.S. Dresselhaus, G. Chen, Z. Ren, High thermoelectric performance of nanostructured bismuth antimony telluride bulk alloys, Science 320 (2008) 634–638.

[22] A. Kumar, U. Singisetti, First principles study of thermoelectric properties of β-gallium oxide, Appl. Phys. Lett. 117 (2020) 262104.

[23] Q. Liu, Z. Chen, X. Zhou, Electronic, thermal, and thermoelectric transport properties of ϵ-Ga_2O_3 from first principles, ACS Omega 7 (2022) 11643–11653.

[24] E. Haque, C. Cazorla, M.A. Hossain, First principles prediction of large thermo-electric efficiency in superionic Li_2SnX_3 (X=S, Se), Phys. Chem. Chem. Phys. 22 (2020) 878.

[25] H. Wang, Q. Qin, J. Yang, Z. Qin, Y. Yao, Q. Wang, M. Hu, First-principles study of electronic, optical and thermal transport properties of group III-IV Monolayer MX (M=Ga, in; X=S, Se), Appl. Phys. 125 (2019) 245104.

[26] Y. Xu, H. Zhang, H. Shao, G. Ni, J. Li, H. Lu, R. Zhang, B. Peng, Y. Zhu, H. Zhu, C.M. Soukoulis, First-principles study on the electronic, optical, and transport properties of Monolayer α- and β-GeSe, Phy. Rev. B 96 (2017) 245421.

[27] X. He, D.J. Singh, P. Boon-on, M. Lee, L. Zhang, Dielectric behavior as a screen in rational searches for electronic materials: Metal pnictide sulfosalts, J. Am. Chem. Soc. 140 (2018) 18058–18065.

[28] M. Wu, D. Sun, C. Tan, X. Tian, Y. Huang, Al-doped ZnO monolayer as a promising transparent electrode material: A first-principles study, Materials 10 (2017) 359.

[29] R. D'Souza, J. Cao, J.D. Querales-Flores, S. Fahy, I. Savi, Electron–phonon scattering and thermoelectric transport in p-type PbTe from first principles, Phys. Rev. B 102 (2020) 115204.

[30] C.E. Ekuma, D.J. Singh, J. Moreno, M. Jarrell, Optical properties of PbTe and PbSe, Phys. Rev. B 85 (2012) 085205.

[31] H. He, R. Orlando, M.A. Blanco, R. Pandey, First-principles study of the structural, electronic, and optical properties of Ga_2O_3 in its monoclinic and hexagonal phases, Phys. Rev. B 74 (2006) 195123.

[32] T. Ouyang, E. Jiang, C. Tang, J. Li, J. Zhong, Thermal and thermoelectric properties of monolayer indium triphosphide (InP_3): a first-principles study, J. Mater. Chem. A 6 (2018) 21532.

[33] A. Soni, V. Gupta, C.M. Arora, A. Dashora, B.L. Ahuja, Electronic structure and optical properties of $CuGaS_2$ and $CuInS_2$ solar cell materials, Sol. Energy 84 (2010) 1481–1489.

[34] Y. Saeed, A. Kachmar, M.A.J. Carignano, Phys. Chem. C 121 (2017) 1399–1403.

[35] G. Kresse, J. Furthmüller, Efficient iterative schemes for ab initio total-energy calculations using a plane-wave basis set, Phys. Rev. B 54 (1996) 11169–11186.

[36] G. Kresse, J. Furthmuller, Efficiency of ab-initio total energy calculations for metals and semiconductors using a plane-wave basis set, Comput. Mater. Sci. 6 (1996) 15–50.

[37] G. Kresse, H. Hafner, Ab initio molecular dynamics for liquid metals, Phys. Rev. B 47 (1993) 558–561.

[38] Blöchl, Projector augmented-wave method, Phys. Rev. B 50 (1994) 17953–17979.

[39] J.P. Perdew, K. Burke, M. Ernzerhof, Generalized gradient approximation made simple, Phys. Rev. Lett. 77 (1996) 3865–3868.

[40] H.J. Monkhorst, J.D. Pack, Special points for Brillouin-zone integrations, Phys. Rev. B 13 (1976) 5188–5192.

[41] L. Chaput, A. Togo, I. Tanaka, G. Hug, Phonon-phonon interactions in transition metals, Phys. Rev. B 84 (2011) 094302.

[42] A. Togo, L. Chaput, I. Tanaka, Distributions of phonon lifetimes in Brillouin zones, Phys. Rev. B 91 (2015) 094306.

[43] A.M. Ganose, J. Park, A. Faghaninia, R. Woods-Robinson, K.A. Persson, A. Jain, Efficient calculation of carrier scattering rates from first principles, Nature Commun. 12 (2021) 2222.

[44] J. Rijnsdorp, G.J.D. Lang, G.A. Wiegers, Preparation, structures, and properties of niobium chalcogenide halides NbX_2Y_2 (X=S, Se; Y=Cl, Br, I), J. Soli. Stat. Chem. 30 (1979) 365–373.

[45] B. Sun, Z. Ma, C. Hea, K. Wu, Anisotropic thermoelectric properties of layered compounds in SnX2 (X=S, Se): a promising thermoelectric material, Phys. Chem. Chem. Phys. 17 (2015) 29844.

[46] W. Rahim, J.M. Skelton, D.O. Scanlon, Ca_4Sb_2O and Ca_4Bi_2O: two promising mixed-anion thermoelectric, J. Mater. Chem. A 9 (2021) 20417–20435.

[47] N. Wang, C. Shen, Z. Sun, H. Xiao, H. Zhang, Z. Yin, L. Qiao, High-temperature thermoelectric monolayer Bi_2TeSe_2 with high power factor and ultralow thermal conductivity, ACS Appl. Energy Mater. 5 (2020) 2564–2572.

[48] M. Gajdoš, K. Hummer, G. Kresse, J. Furthmüller, F. Bechstedt, Linear optical properties in the projector-augmented wave methodology, Phys. Rev. B 73 (2006) 045112.

[49] A. Bafekry, B. Mortazavi, M. Faraji, M. Shahrokhi, A. Shafique, H.R. Jappor, C. Nguyen, M. Ghergherehchi, S.A.H. Feghhi, Ab initio prediction of semicon-ductivity in a novel two-dimensional Sb_2X_3 (X=S, Se, Te) monolayers with orthorhombic structure, Sci. Rep. 11 (2021) 10366.